Ultramicroscopy 205 (2019) 70–74

Contents lists available at ScienceDirect

Ultramicroscopy

journal homepage: www.elsevier.com/locate/ultramic

# Performance of plastic electron optics components fabricated using a 3D printer

Phillip Wiebe, Peter Beierle, Hua-Chieh Shao, Bret Gergely, Anthony F. Starace, Herman Batelaan*

*Department of Physics and Astronomy, The University of Nebraska, Lincoln, Nebraska 68588-0299, United States*

A B S T R A C T

We show images produced by an electron beam deflector, a quadrupole lens and a einzel lens fabricated from conducting and non-conducting plastic using a 3D printer. Despite the difficulties associated with the use of plastics in vacuum, such as outgassing, poor conductivity, and print defects, the devices were used successfully in vacuum to steer, stretch and focus electron beams to millimeter diameters. Simulations indicate that much smaller focus spot sizes might be possible for such 3D-printed plastic electron lenses taking into account some possible surface defects. This work was motivated by our need to place electron optical components in difficult-to-access geometries. Our proof-of-principle demonstration opens the door to consider 3D-printed electron microscopes, whose reduced cost would make such microscopes more widely available. Potentially, this may have a significant impact on electron beam science and technology in general and electron microscopy in particular.

## 1. Introduction

In electron optics it is both time-consuming and costly to machine electron optical elements (such as einzel lenses and deflectors). This is one reason why electron microscopes and dedicated matter optics experiments are comparatively expensive. It is therefore desirable to create a faster and more cost-effective production method for such components. In order to avoid the need for assembly, it is desirable for these components to be monolithic constructions. A promising way to meet these criteria is to employ a 3D printer. However, there are some necessary conditions that must be met. These include being able to print using both conducting material, to create the required electric potentials, and insulating material, to keep the elements electrically isolated. Additionally, the outgassing of the printing material must be kept to a minimum to maintain the system's vacuum quality. There is also the key issue of how the 3D print quality affects the time response, the resolution, and the focus of the electron optical element. Finally, despite the fact that advanced printers have been developed that can meet some of these requirements [1–4], that outgassing information is available [5,6], and that molecular beams have been successfully manipulated with a 3D-printed electroplated beam splitter [7], we are not aware of 3D-printed plastic electron optics devices for charged particle beam applications.

In this letter, we provide a proof-of-principle demonstration that most of the necessary requirements can be met through our fabrication and testing of a 2D-deflector, an electrostatic quadrupole lens, and an einzel focusing lens. These were fabricated using a LULZBOT TAZ 6 printer with a dual extruder tool-head (v2) that can switch between conducting filaments (Proto-Pasta PLA conductive CDP 12805) and non-conducting filaments (Proto-Pasta Everyday PLA). The electron optics devices were printed in their entirety as one piece. We demonstrate the functionality of the deflector and quadrupole lens in a simple electron-optics setup. The encouraging results obtained prompted us to speculate that such electron optical elements might be used in modest-resolution electron microscopes. However, a concern was that the roughness and potential asymmetry of the 3D-printed lens may prohibit this. Therefore, we have carried out and report here results of a basic theoretical model and simulations on some effects causing aberration, in particular corrugation, as that is typical of 3D-printing. These simulation results indicate that, despite such lens aberrations, a focal spot of less than 100 nm might be possible, which would approach the resolution of environmental inspection electron microscopes. We caution that further study is required to investigate the potential deleterious effects of printing deformities, local charging of the plastic, and local outgassing. We note that post-processing can be investigated. For example, the use of a warm metal cylinder pressed into the plastic einzel focusing lens could correct for out-of-roundness, reducing parasitic abberation.

* Corresponding author at: Theodore Jorgensen Hall 208, 855 N 16th Street, Lincoln, NE 68588-0299, United States.
*E-mail addresses:* phillip.wiebe@huskers.unl.edu (P. Wiebe), hbatelaan2@unl.edu (H. Batelaan).

https://doi.org/10.1016/j.ultramic.2019.05.013
Received 14 September 2018; Received in revised form 25 May 2019; Accepted 29 May 2019
Available online 30 May 2019
0304-3991/ 

## 2. Experiment with electron deflector, quadrupole lens, and focusing lens

A limitation of these monolithic devices is the conductive material's tendency to leak through to the nonconductive material, owing to the way the printing material is deposited and shaped. This leakage defeats the electrical isolation of the devices. Specifically, solid Polylactic Acid (PLA) is pushed through an extruding nozzle in a hot liquid state, whereupon it cools back into solid form on a platform. Conductive PLA has a different melting point than nonconductive PLA, and the printing nozzles in the dual-nozzle printing head were separately heated to the factory recommended temperatures. Various nozzle diameters were also tested to optimize the resolution and avoid the aforementioned failure mode. The standard 1.5 mm nozzle size resulted in leakage, but use of a 1.2 mm nozzle solved this problem. Finally, in order to avoid having the printed objects deform under the pressure of their own weight, cooling of the deposited material needs to be considered. A desktop fan used during the printing process provided sufficient cooling.

After fine-tuning the printing parameters, an electron deflector (which can steer the electron beam in both transverse directions), an electrostatic quadrupole lens (with a hyperbolic electrode design), and an einzel focusing lens were fabricated. These 3D-printed electron devices are shown in Fig. 1. The plates, hyperbolas, and cylinders are insulated from their housing with a resistance exceeding 10 MΩ. The resistance from the electrical wires to the deflector plates and quadrupole elements is 10 kΩ so that a constant potential can be maintained.

To test the fabricated device components, they were installed in a vacuum chamber and arranged into a simple electron optics setup, as shown in Fig. 2. For the deflector and quadrupole, a 100 eV electron beam was emitted from a tungsten filament cathode (Kimball Physics ES-026R) with a Wehnelt cylinder to enhance the forward transmission, producing an initial emission current of 1.6 $\mu$A. A 200 μm collimation aperture was placed 32.5 cm downstream. The electrons then passed through 3 cm long deflection plates. The beam then traveled another 27 cm to reach the quadrupole lens, and finally was detected using a chevron multichannel plate and phosphorous screen (BVS-1-OPT01), which is imaged with a CCD camera and image acquisition software. For the einzel lens, a 300 eV electron beam was used, a 100 μm collimation aperture, and a large diameter edge aperture to reduce secondaries was used. Without the aperture, electrons from the source would produce secondary electrons from walls that travel unimpeded to the detector to produce a significant background signal. The round aperture had thin walls (0.1 mm) to reduce secondary emission from the aperture itself.

The complete testing rig was placed in a regular high vacuum chamber and pumped down with a turbo and roughing pump combination. With the printed elements installed, their outgassing was limited so that the vacuum system was able to pump down in 24 hours to a final pressure of $3.9 \times 10^{-7}$ Torr, while without the plastic elements a final pressure was $3.8 \times 10^{-7}$ Torr. The effective pump speed was determined from the pump down rate at 58 L/s (using a turbo pump with a nominal pump speed of 240 L/s). With an estimated surface area of the plastic lens element of 562 $cm^2$, the outgassing rate is estimated at $1 \times 10^{-9}$ Torr L/cm$^2$ s, consistent with known values [8]. Note that in the direct vicinity of the plastic surfaces the pressure may be higher due to outgassing. The pressure implies that the mean free path is about 10 m. Considering that the entire path length is less than the vacuum tube length ~ 0.60 m, the electron beam is unimpeded and the 3-D printed devices do not outgas to a detrimental degree for basic electron optics tests.

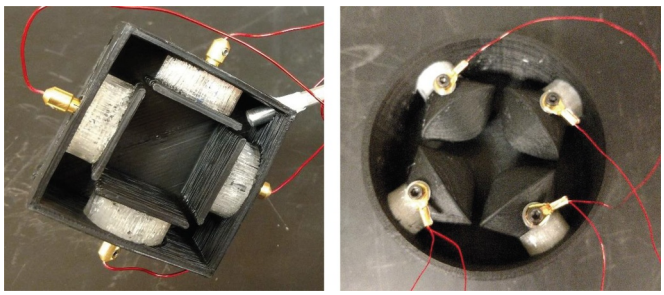

**Fig. 1.** 3D-printed electron optics components. (Left) An electron deflector. (Right) An electron quadrupole lens. For both electron optics components, the lighter-colored plastic is insulating and the grey-colored plastic is conducting.

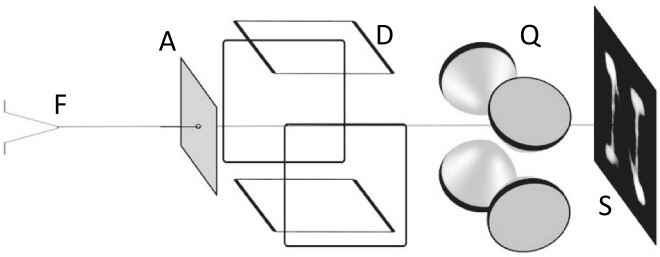


**Fig. 2.** Schematic of a simple 3-D printed electron optics setup. A heated filament (F) produces an electron beam that is collimated by an aperture (A), passes through a 2-D deflector (D) that is scanned at 10 kHz, and passes through a quadrupole lens (Q) that stretches the image as detected on a multi-channel plate screen (S).

When observing the electron beam with the MCP, the imaged beam spot maintained its narrowness with time. This indicates that there is no appreciable charging taking place in the system. To demonstrate the deflector's functionality, the letter "N" of 10 mm size along its diagonal was written on the fluorescent screen using a manually programmed master-slave pair of SRS-function generators running at 10 kHz (Fig. 3). The available MCP had burn-in spots which caused some variation in the brightness of the image. A constant voltage difference of $\Delta V$ on the deflection plates gives an estimated displacement of the electron beam on the detector screen of $h = (ed)/(mv^2)\Delta V$, where $e$ is the electron charge, $d$ is the distance from the deflection plate to the phosphorous screen, $m$ is the electron mass and $v$ is the electron velocity. From the observed deflection of ~ 3.1 mm, the estimation indicates that the deflection plate holds a voltage difference of $\Delta V_A = 4.1$ V. The agreement with the applied voltage of $\Delta V_A = 4.4$ V is reasonable, given that fringing fields are ignored in the estimation.

To test the quadrupole lens, voltage differences of about ± 1 V were applied to one set of diagonal hyperbolic electrodes (see Fig. 2) while the deflector plates were scanning. The result was that the "N" at the detector was stretched along the positively-biased diagonal, and compressed along the negatively biased diagonal (Fig. 3). A rough estimate of the degree of expected spatial distortion can be computed from,

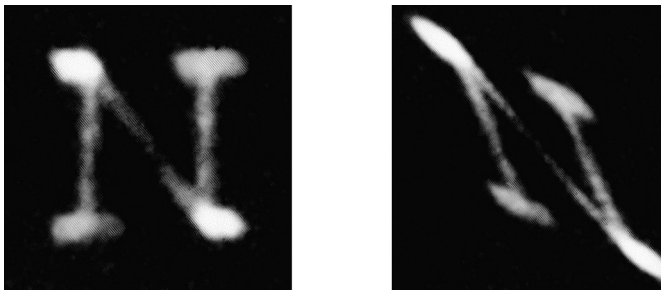

**Fig. 3.** Electron images. (Left) The letter "N" of 10 mm size along its diagonal is written with a plastic 3D-printed electron deflector. (Right) The letter "N" is stretched along one diagonal and compressed along the other diagonal using a quadrupole lens.

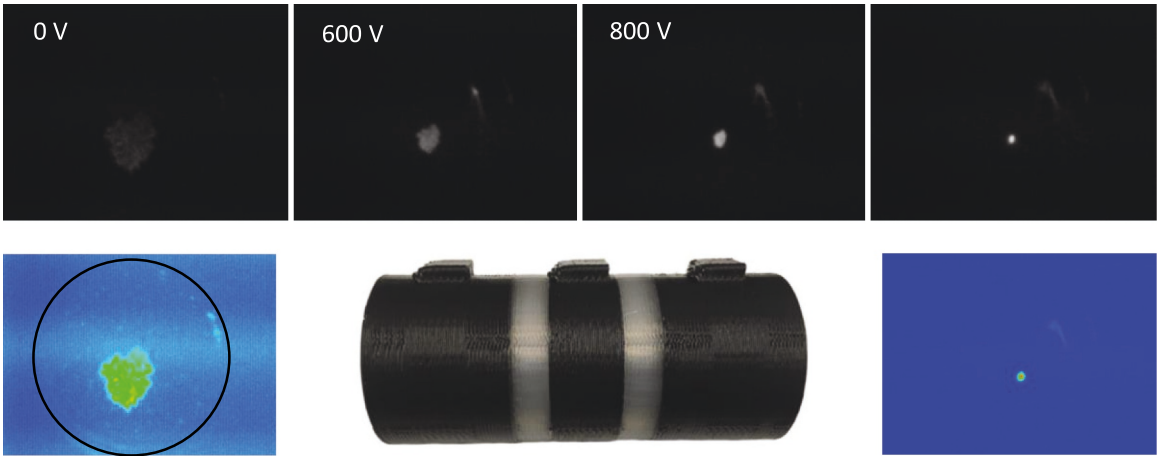


**Fig. 4.** 3D-printed electron lens. (Bottom middle) A photograph of the einzel lens. The light grey areas are non-conducting plastic, the black areas are conducting plastic. (Top row, from left to right) Starting from 0 V, increasing voltages applied to the middle section of the lens focusses an electron beam from an unfocussed diameter of 5 mm to 0.5 mm. (Left and right bottom) The beam image is reproduced in false color and the 20 mm diameter detector circumference is indicated.

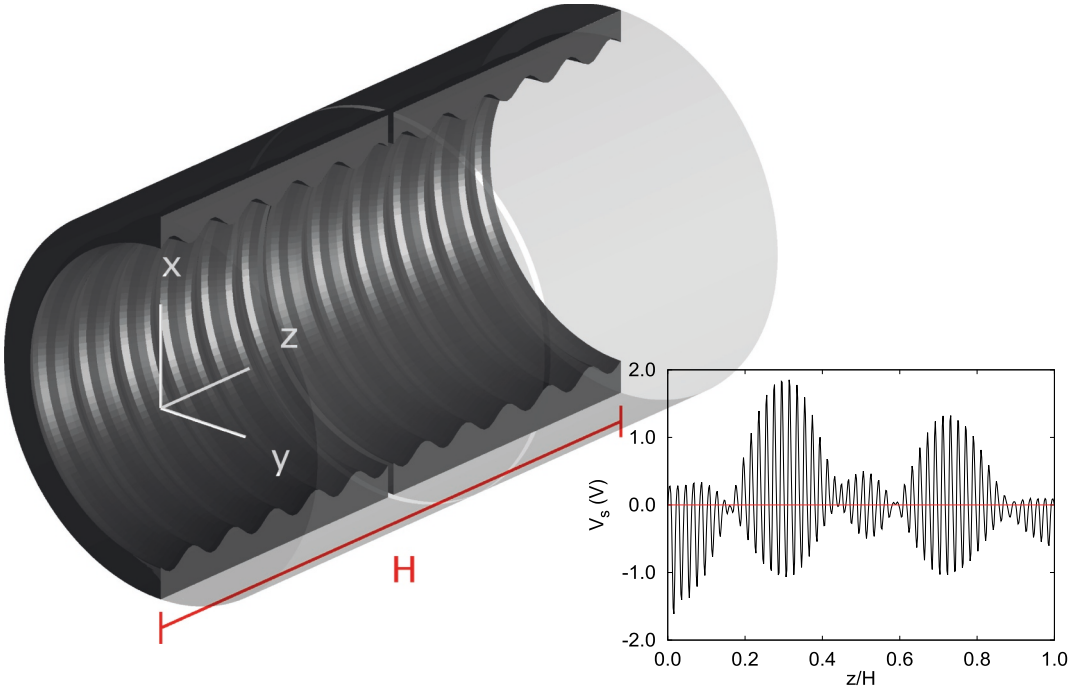


**Fig. 5.** Illustration of surface defects of the side of a two-cylinder lens. Corrugation on the side of the cylinder (not drawn to scale) due to a flaw in 3D printing can be seen in the cutaway. The inset shows an example of a surface patch potential at which the surface deviates from that of a perfect conductor [see Eq. (4)].

$$S \equiv \frac{M_e}{M_c} = \frac{1+\Delta}{1-\Delta}, \tag{1}$$

where the squeezing factor $S$ is defined as the ratio between the magnification factor in the elongation direction $M_e$ over the magnification factor in the compression direction $M_c$ and $\Delta = eV_0 l_1 l_2 L/[r_0^2 E(l_1 + l_2)]$. This result can be obtained using the impulse approximation and assuming a uniform saddle-point potential over the length of the quadrupole. The applied voltage difference $V_0$ is about 1 V, the quadrupole length $L$ is 0.04 m, the electrode distance $2r_0$ is 20 mm, the electron energy $E$ is 100 eV, the distance from the deflection plates to the quadrupole, $l_1$, is 0.3 m and that from the quadrupole to the detector, $l_2$, is 0.3 m, and the electron charge is given by $e$. The measured values for the image are $M_e = 1.45$ and $M_c = 1.70$, giving $S = 2.5$. The theoretical value is $S = 4$, which is reasonable agreement given the crude approximation used for our estimate. This demonstration, which was motivated by a need to place such elements in hard-to-reach places, led us to speculate that 3-D printed lenses may be suitable for electron microscopes [9]. As a first step, we attempted another proof-of principle demonstration, and a three-element einzel lens was printed in the manner described above (Fig. 4).

To test the einzel lens, first the shadow of the small aperture was observed with the einzel lens turned off. The irregular-shaped pattern had a width of about 5 mm. Increasing the voltage on the central cylindrical electrode from 0 V to 1042 V produces a focus of 0.5 mm. The central electrode voltage was chosen positive so that the lens was run in "accel-decel" mode [10]. For comparison, false color images are included at the same scale, which show the rim of our 20 mm diameter detector (also indicated with an added circle). At the electron energies available in our test rig, no further improvement is expected due to

limited magnetic field shielding (5 mG/cm gradients were measured).

## 3. Theoretical analysis of surface defects on focusing lens performance

Surface defects caused by imperfections in 3D printing can impair the performance of lenses. In the following, we present simulations that show the effects of such surface defects as corrugation and a patch potential on the focal properties of an einzel lens. Other aberrations, including parasitic ones, are expected in our current system. These can be larger and of lower order than the ones considered here [11]. The motivation for considering corrugation and patch potentials is that they can be problems that are particular to 3D-printing with plastic, and estimates due to these effects are not readily accessible in the literature.

We consider a two-cylinder lens with zero gap and end caps, so that the lens system can be analyzed analytically using the Laplace equation. The cylinder is divided into equal halves whose potentials are kept at zero and $V$, respectively (Fig. 5). The general form of the scalar potential (in cylindrical coordinates) is

$$\Phi(r, \phi, z) = \sum_{mn} A_{mn} I_m(k_n r) e^{im\phi} \sin(k_n z) + V\frac{z}{H}, \tag{2}$$

where $A_{mn}$ are the expansion coefficients, $I_m(\cdot)$ is the modified Bessel function of the first kind [12], $k_n \equiv n\pi/H$, and $H$ is the length of the lens. The second term is the potential of two infinite parallel plates, which accounts for the boundary condition (BC) at the end caps. The first term takes account of the potential resulting from the BCs on the side of the cylinder, such as a finite radius with or without surface defects. Since the modified Bessel function grows exponentially $I_m(x) \sim e^x/\sqrt{2\pi x}$ as $x \to \infty$, $1/k_n$ characterizes the decay length of the longitudinal mode $n$ in the radial direction. Therefore, one may anticipate that any high frequency mode induced by the BCs on the side of the cylinder has little consequence near the axis (*i.e.*, $r \ll 1/k_n$).

First, we consider the corrugation on the side of the cylinder (Fig. 5) to simulate periodic imperfections due to printing (lines of molten plastic are deposited one after another with a constant stepsize). The corrugation is assumed to be axially symmetric, so all $m \neq 0$ terms in $\Phi$ vanish. Moreover, the fluctuation is modeled as a sinusoidal oscillation with frequency $k_c \equiv c\pi/H$, $c \in \mathbb{R}$:

$$R(z) = R_0 + \epsilon \sin(k_c z), \tag{3}$$

where $R_0$ is the nominal radius of the cylinder, and $\epsilon$ is the amplitude of the fluctuation. The amplitude $\epsilon$ and wavelength $\lambda_c = |2\pi/k_c|$ of the fluctuation are assumed to be much smaller than the dimensions of the lens (*i.e.*, $\epsilon \ll R_0$ and $\lambda_c \ll H$). We solve for $A_{0,n}$ by applying the BC (3); then the electron trajectories are calculated using the non-relativistic equation of motion and the Runge-Kutta method. Fig. 6(a) and (b) compare the electron trajectories of smooth (*i.e.*, $\epsilon = 0$) and corrugated surfaces. The right panels show the trajectories near the foci. The parameters of the lens are $V = 4$ kV, $H = 20$ mm, $R_0 = 5$ mm, $\epsilon = 100\,\mu$m, and $\lambda_c \approx 396\,\mu$m ($c = 101$). The initial velocity of electrons is $4 \times 10^7$ m/s in the $z$ direction. One can see that the focus of the corrugated surface [Fig. 6(b)] shifts toward the left, but the envelope of the trajectories and the size of the focal spot change only slightly.

Next, we study effects of a surface patch potential. The patch potential $V_s$ is modeled as a superposition of oscillating potentials with amplitudes $V_n$:

$$V_s(\phi, z) = \sum_n V_n \cos(\phi) \sin(k_n z). \tag{4}$$

The axial symmetry of the lens is broken by the azimuthal dependence $\cos(\phi)$ which leads to a non-zero electric field on the axis. Here we only consider the $m = 1$ term in Eq. (2), as an example, because it is the lowest order term that breaks the axial symmetry, and the only term that gives a non-zero field on axis. We randomly choose 11 components $V_n$ centered at $n = 101$ with magnitude $|V_n| < 0.5$ V. The inset of Fig. 5

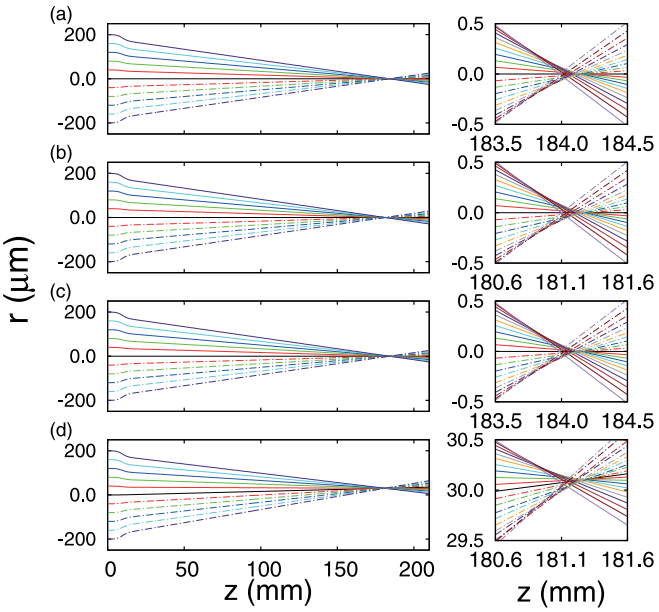


**Fig. 6.** Comparison of electron trajectories passing through cylinder lenses without and with surface defects: (a) smooth surface, (b) corrugated surface, (c) surface patch potential, and (d) combination of corrugation and patch potential. The right panels show the trajectories near the foci. See text for the configuration of the lens and the parameters used in the simulations.

shows an example of the patch potential at $\phi = 0$ as a function of $z$, and Fig. 6(c) shows the trajectories resulting from such a surface defect. One can see that the trajectories are essentially the same as those for a smooth surface [Fig. 6(a)]. Even though the axial symmetry is broken, no appreciable transverse displacement of the focus is observed.

Lastly, we combine both the corrugation and patch potential, whose results are presented in Fig. 6(d). Here one sees that the focus is not only shifted horizontally, as seen in Fig. 6(b), but also deviates from the axis. The effect of a patch potential is amplified by the corrugation, yet individually they have only small effects, and moreover the focal width remains largely unaffected.

In order to understand why the interplay of corrugation and a patch potential renders significant effects, we inspect the behavior of some mode $\Phi_{mn}$ on the side of the cylinder:

$$\Phi_{mn}(\phi, z) \equiv I_m(k_n R(z)) e^{im\phi} \sin(k_n z), \tag{5}$$

where the modified Bessel function can be approximated as

$$I_m(k_n R(z)) \simeq I_m(k_n R_0) + k_n \epsilon \sin(k_c z) I'_m(k_n R_0). \tag{6}$$

The first term corresponds to the mode of the smooth surface, while the second term accounts for the first-order perturbation of $\Phi_{mn}$ involving a new frequency $k_c$ that is introduced in the longitudinal mode $n$ by the corrugation. Substituting Eq. (6) into Eq. (5), one can see that the heterodyning of $k_c$ and the natural frequency $k_n$ yields new frequencies $k_{n-c}$ and $k_{n+c}$. In other words, the corrugation effectively shifts $\Phi_{mn}$ such that it behaves like $\Phi_{m,n-c}$ and $\Phi_{m,n+c}$. Therefore, once some surface potential oscillates about the same frequency of the corrugation (*i.e.*, $n \approx c$), the surface patch potential appears as a low frequency perturbation which, in turn, is more significant to the motion of electrons.

## 4. Summary and conclusion

In summary, we have successfully produced functioning electron optical components using conductive and non-conductive plastics with a commercial 3-D printer. The devices were an electron deflector, an electron quadrupole lens, and an einzel lens. We have also analyzed a simple electron optics lens. The simulated focal width of the electron

beam is less than 100 nm even when reasonably-sized surface corrugations and asymmetric patches are taken into account. This is by no means a complete study of deleterious effects, but highlights some problems specific to 3D-printed plastic lenses. As compared to existing electron microscopes, such a performance is modest but nevertheless better than that of optical microscopes and is comparable to those used in environmental electron microscopes. The present experimental demonstration of plastic 3D-printed electron optics parts and the rather optimistic positive results of the theoretical analysis of the effects of some possible fabrication flaws provide a tangible step toward developing an affordable electron microscope that would be accessible to a larger customer group, including, for example, high schools.

## Acknowledgements

This work was supported in part by the U.S. National Science Foundation under Grant Nos. PHY-1602755 (P.W., P.B., and H.B.) and PHY-1505492 (H.-C.S. and A.F.S.) The numerical simulations were completed utilizing the Holland Computing Center of the University of Nebraska, which receives support from the Nebraska Research Initiative.

## Supplementary material

Supplementary material associated with this article can be found, in the online version, at 10.1016/j.ultramic.2019.05.013

## References

[1] D.N. Silva, Dimensional error in selective laser sintering and 3D-printing of models for craniomaxillary anatomy reconstruction, J. Cranio-Maxillofac. Surg. 36 (2008) 443–449, https://doi.org/10.1016/j.jcms.2008.04.003.
[2] L.A. Hockaday, Rapid 3D printing of anatomically accurate and mechanically heterogeneous aortic valve hydrogel scaffolds, Biofabrication 4 (2012) 035005–1–12, , https://doi.org/10.1088/1758-5082/4/3/035005.
[3] C. Zhang, N.C. Anzalone, R.P. Faria, J.M. Pearce, Open-source 3D-printable optics equipment, PLoS One 8 (2013) e59840–1–13, , https://doi.org/10.1371/journal.pone.0059840.
[4] B.C. Gross, Evaluation of 3D printing and its potential impact on biotechnology and the chemical sciences, Anal. Chem. 86 (2014) 3240–3253, https://doi.org/10.1021/ac403397r.
[5] Outgassing data for selecting spacecraft materials, [Online]. Available: https://outgassing.nasa.gov.
[6] A.P. Povilus, Vacuum compatibility of 3D-printed materials, J. Vac. Sci. Technol. A 32 (2014) 033001–1–3, , https://doi.org/10.1116/1.4873556.
[7] S.D.S. Gordon, A. Osterwalder, 3D-printed beam splitter for polar neutral molecules, Phys. Rev. Appl. 7 (2017) 044022–1–7, , https://doi.org/10.1103/PhysRevApplied.7.044022.
[8] Z. Sun, L.F. Velsquez-Garca, Monolithic FFF-printed, biocompatible, biodegradable, dielectric-conductive microsystems, J. Microelectromech. Syst. 26 (6) (2017).
[9] The focusing lens section was added upon request by anonymous referee.
[10] H. Liebl, Applied Charged Particle Optics, Springer-Verlag, Berlin, Heidelberg, 2008. ISBN-978-3-540-71925-0
[11] H. Rose, Geometrical Charged-Particle Optics, Springer-Verlag, Berlin, Heidelberg, 2009. ISBN 978-3-540-85916-1
[12] M. Abramowitz, I.A. Stegun (Eds.), Handbook of Mathematical Functions with Formulas, Graphs, and Mathematical Tables, Dover, New York, 1972. ISBN-13: 978-0-486-61272-0